Nanoscale

Accepted Manuscript

This article can be cited before page numbers have been issued, to do this please use: T. S. Santra, S. Kar, C. Chen, J. Borana, T. Chen, M. Lee and F. Tseng, *Nanoscale*, 2020, DOI: 10.1039/D0NR01792B.

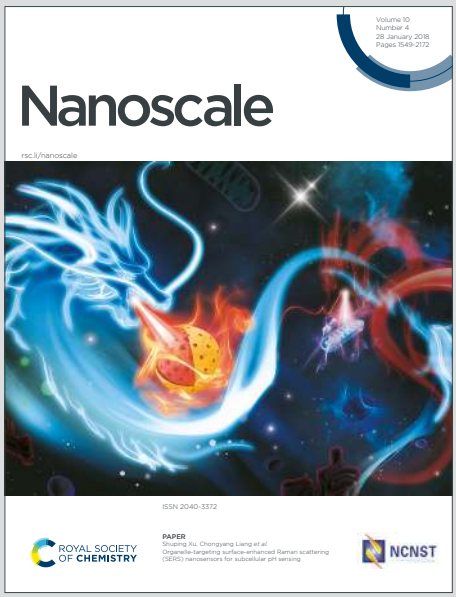

ROYAL SOCIETY OF CHEMISTRY

rsc.li/nanoscale

Nanoscale

View Article Online
DOI: 10.1039/D0NR01792B

ARTICLE

Near-infrared nanosecond-pulsed laser-activated high efficient intracellular delivery mediated by nano-corrugated mushroom-shaped gold-coated polystyrene nanoparticles

Received 00th January 20xx,
Accepted 00th January 20xx

DOI: 10.1039/x0xx00000x

Tuhin Subhra Santra,[a,b,#,*] Srabani Kar,[c,#] Te-Chang Chen,[d] Chih-Wei Chen,[e] Jayant Borana,[f] Ming-Chang Lee[d,g] and Fan-Gang Tseng[b,f,h,*]

Here, efficient intracellular delivery of molecules with high cell viability is reported using nanosecond-pulsed laser-activated plasmonic photoporation mediated by high-aspect-ratio nano-corrugated mushroom-shaped gold-coated polystyrene nanoparticles (nm-AuPNPs) at near-infrared wavelength. Upon laser illumination, nm-AuPNPs exhibit greater plasmonic extinction than spherical AuPNPs, which increase their energy efficiency and reduce the necessary illumination of light, effectively controlling cell damage and improving delivery efficiency. Nm-AuPNPs exhibit surface plasmon absorption at near infrared region with peak at 945 nm. Pulsed laser illumination at this plasmon peak triggers explosive nanobubbles, which create transient membrane pores, allowing the delivery of dyes, quantum dots and plasmids into the cells. The results can be tuned by laser fluence, exposure time, molecular size and concentration of nm-AuPNPs. The best results are found for CL1-0 cells, which yielded a 94% intracellular PI dye uptake and ~100% cell viability at 35 mJ/cm^2 laser fluence for 945 nm wavelength. Thus, the presented approach has proven to have an inevitable potential for biological cell research and therapeutic applications.

Introduction

Introducing foreign biomolecules into targeted living cells efficiently without compromising cell viability is a challenging, yet critical task for many biological and therapeutic applications.[1-2] Researchers have developed many transfection techniques, including the use of viral vectors,[3] chemical methods such as basic proteins, complexes with lipids and calcium phosphate,[4] and physical methods such as electroporation,[5-6] lipid-mediated entry into cells,[7] microinjection,[8] jet injection,[9] and sonoporation.[10] Among these methods, chemical formulation, such as polymers and cationic lipids, encounter targeting efficiency issues, endocytic degradation, and the need for cell-specific formulation.[11-12] Moreover, limitations of using viral vectors for gene transfer include mutagenicity, triggering an immune response, toxicity, and its high cost.[13-14] While physical methods, such as ultrasound, laser irradiation, and electroporation, are effective substitutes for gene transfer without these limitations,[15] are often insufficient.[16] For example, while microinjection directly injects compounds into cells, it requires a highly skilled person to operate the task, which means the delivery throughput is low. In recent years, sonoporation or cellular sonication has been employed to permeabilize cell plasma membranes before delivery. The acoustically induced cavitation bubbles form microjets and shockwaves that create transient pores on the cell membrane. However, strong shear forces cause cell damage or toxicity.[17] In contrast, electroporation techniques prove advantageous, owing to their operational ease, short process time, low toxicity, and better-electroporated size control to reduce cytosolic leakage components.[5-6] However, the process encounters issues such as pH variation, electric field distortion and thermal effect, due to the application of micro- to

[a] Department of Engineering Design, Indian Institute of Technology Madras, India
[b] Institute of Nanoengineering and Microsystems, National Tsing Hua University, Taiwan.
[c] Department of Electrical Engineering, University of Cambridge, Cambridge, UK
[d] Institute of Photonics Technology, National Tsing Hua University, Taiwan
[e] Institute of Molecular Medicine, National Tsing Hua University, Taiwan
[f] Department of Engineering and System Science, National Tsing Hua University, Taiwan
[g] Department of Electrical Engineering, National Tsing Hua University, Taiwan
[h] Division of Mechanics, Research Center for Applied Sciences, Academia Sinica, Taiwan

# Equal contribution
* Corresponding authors: tuhin@iitm.ac.in; fangang@ess.nthu.edu.tw
† Footnotes relating to the title and/or authors should appear here.
Electronic Supplementary Information (ESI) available: [details of any supplementary information available should be included here]. See DOI: 10.1039/x0xx00000x

millimeter-sized large electrodes, which induces a strong current that deteriorates cell viability.[18-19]

In recent years, photoporation has emerged as a promising physical method for intracellular delivery. In this technique, a high-intensity laser applied to the cell membrane creates permeable membrane pores that can deliver biomolecules. Using a multiphoton process and submicron membrane pores, femtosecond laser pulses can create low-density plasma on the cell membrane surface,[20-21] achieving a maximum of 80% to 90% cell-specific transfection efficiency.[22-23] Continuous-wave lasers heat the cell membrane to form permeable pores with less than 30% transfection efficiency,[24-25] whereas, nanosecond laser pulses induce cavitation bubbles with a high transfection efficiency of up to 88%.[26-27] In recent years, nanoparticle-mediated techniques have been introduced to further enhance the coupling efficiency of photonic energy into cell poration.[28-29] For example, lasers can interact with gold nanoparticles (AuNPs) to produce nanoscale energy deposition to the surrounding medium through light amplification and heat generation. Among various nanoparticles (NPs), AuNPs possess many valuable properties, such as surface plasmon resonance, high chemical stability, biocompatibility, convenient surface bioconjugation with molecular probes and low toxicity.[28, 30-31] Different gold nanostructures such as nanocrescents, nanorods, nanoshells, nanocages, and half nanoshells have excellent photothermal properties.[30,32-33] Due to the high surface plasmon resonance of AuNPs, upon pulsed laser illumination of the cell membrane-AuNPs interface, high photoporation efficiency can be achieved when large amounts of cells are clumped together.[28-29] When a high-intensity nanosecond (<10 ns) laser pulse interacts with AuNPs, the temperature increases rapidly and the surrounding medium is vaporized to form plasmonic nanobubbles (PNBs) or photothermal vapor nanobubbles (VNBs) across the AuNPs surface.[33-34] After the bubbles collapse, the generated cavitation and stress waves cause heat transfer from the AuNPs to the surrounding area. The amount of generated heat depends on particle size and shape, aggregation of particles, laser intensity, and wavelength and pulse duration. However, in case of a very short lifetime (<1 μs) of PNBs, the heat transferred from the AuNPs to the surrounding medium beyond immediately created localize PNBs is negligible and all irradiated energy from the AuNPs is transferred as mechanical energy.[35-36] When this mechanical energy exceeds the cell membrane threshold values, transient membrane pores are created, allowing biomolecules to be gently delivered into the cells.[35-36] This approach was followed by Xiong et al, who used spherical AuNPs to achieve best delivery efficiency of 85% (FITC-dextran) and cell viability ~ 90% at very high laser fluence of 2 J/cm^2.[37] However this energy is high enough by means of cell damage and energy savings, and thus still there is free room to reduce the energy and improve the delivery efficiency and cell viability. In addition, most of the studies used visible wavelength for cell poration.[38,39] Whereas, it is a well-established fact that maximum penetration of electromagnetic radiation in biological tissue occur approximately from 650 nm to 1350 nm-the near infrared (NIR) range; therefore possesses great promise for in vivo applications.[40,41] Furthermore, NIR range is highly biocompatible and photothermal damage is much less than UV and visible range. Especially NIR range is an emerging field in photothermal therapy. Therefore it is highly demanding to achieve optoporation and cell penetration in NIR. In the present study, our goal is to establish a pathway for utilizing NIR range with lower fluence for cell optoporation. With this background, we aim to shift operating wavelength towards NIR by using high-aspect-ratio nano-corrugated mushroom-shaped gold-coated polystyrene nanoparticles (nm-AuPNPs).

Compared to spherical metal particles, high-intensity surface plasmon can be achieved on non-spherical metal NPs, such as nano triangles and nanorods with sharp edges.[42-43] In our previous articles, we showed the fabrication of high-aspect-ratio nm-AuPNPs, which enhanced the optical hot-spot area, resulting in surface-enhanced Raman spectra (SERS).[44-45] Here, we utilized these nm-AuPNPs as a mediator and applied the nanosecond-pulsed laser to achieve highly efficient intracellular delivery of cargo molecules with high cell viability. After illumination of the laser pulse on nm-AuPNPs (generating ~120-130 hot spots/particle), light absorption increased on the hotspots, resulting in higher production of surface plasmon across the horizon of nm-AuPNPs compared to spherical AuPNPs. Consequently, nm-AuPNPs transferred higher energy to generate PNBs, following a highly efficient intracellular delivery without any cell damage. The best delivery results ware optimized at 945 nm with delivery efficiency 94% (PI dye uptake) and cell viability ~100%, at laser fluence of 35 mJ/cm^2 (for spherical AuPNPs, we obtained a delivery efficiency of 42% and cell viability of 91% at 35 mJ/cm^2) for lung cancer (CL1-0) cells. Moreover, we found molecular uptake efficiency and cell viability depend on laser fluence, exposure time, molecular size and concentration of nm-AuPNPs. Using pulsed laser-assisted photoporation technique, we successfully delivered dyes, quantum dots (QDs) and different plasmids into lung cancer (CL1-0), gastric cancer (AGS) and P-19 embryonic stem cells, with minimum laser fluence (25 mJ/cm^2 - 35 mJ/cm^2) and 30 seconds exposure time at 516 nm. Therefore our methods pave a way to achieve high efficient intracellular delivery with high cell viability at much lower energy.

Results and discussion

nm-AuPNPs mediated intracellular delivery

Fig. 1 shows the schematic experimental procedure for nm-AuPNPs mediated intracellular delivery using a nanosecond-pulsed laser with repetition rate 10 Hz. After we cultured cells overnight in an incubator (37°C with 5% CO_2), polyethylene

glycol (PEG) mediated nanoparticles were placed into the cell culture dish for an hour before the experiment and washed the unbound nm-AnPNPs from the cell surface using phosphate buffer saline (PBS). Then cell-impermeable cargo molecules (Fig. 1 (b)) were introduced into the dish right before the experiment. Due to the nanosecond-pulsed laser illumination of the nm-AuPNPs (Fig. 1 (c)) on the cell membrane, electromagnetic field enhancement occurred near the nano-corrugated edges, resulting in a lightning-rod effect, also known as optical hotspots. The resonantly excited optical hotspots generated local heat, causing a rapid temperature enhancement and subsequent formation of PNBs surrounding the nm-AuPNPs-cell membrane interface. After PNBs formed, they rapidly grew, coalesced, and collapsed to induce an explosion, which caused a strong fluid flow at the nm-AuPNPs-cell membrane interface. After PNBs collapsed, the generated cavitation and stress wave transferred heat from the nm-AuPNPs to the nano-restricted region of the cell membrane.[37]

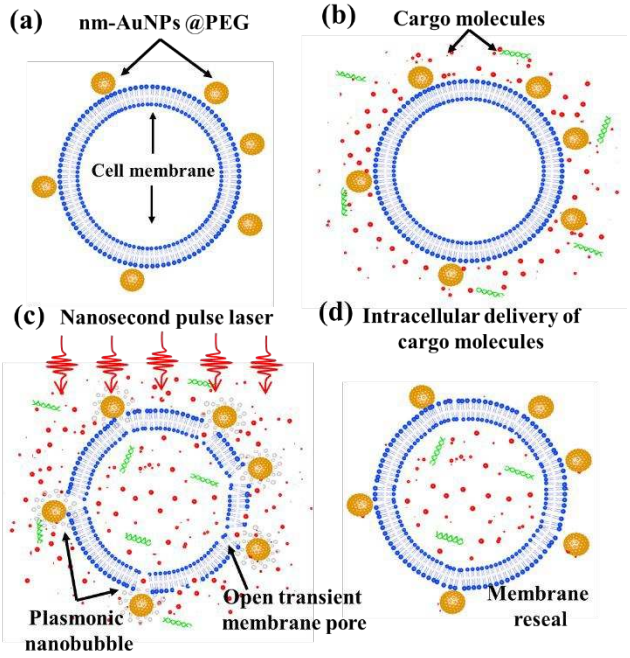

Fig. 1. Schematic overview of photoporation procedure for intracellular delivery (a) cells were incubated with PEG mediated nm-AuPNPs for attachment onto the cell membrane (b) cell surface was washed to remove unbound nm-AuPNPs and then cargo molecules were added just prior to laser exposure (c) nanosecond pulse laser-induced plasmonic nanobubbles formation at nm-AuPNPs and cell membrane interface resulting in transient pore formation into the cell membrane (d) successful intracellular delivery of cargo molecules with membrane reseal.

Furthermore, nanosecond-pulsed laser exposure (pulse duration ~5 ns) results in PNBs having very short lifetime (<1 µs), which is in turn beneficial for negligible heat transfer from nm-AuPNPs to the cell membrane.[35-36] Therefore, almost all irradiated energy from the nm-AuPNPs was transferred as mechanical energy, in the form of strong fluid flows, which disrupted the plasma membrane forming transient membrane pores, allowing the delivery of cargos from outside to inside the cell (Fig.1 (c)). After the cargo was delivered, the cell membrane resealed again, maintaining cell viability (Fig. 1 (d)). The transient pore formation on the cell membrane depends on laser fluence and the concentration of nm-AuPNPs. A detailed fabrication process of nm-AuPNPs is provided in Supplementary Fig. S1. Fig. 2 (a) and Fig. S2 shows the scanning electron microscopy (SEM) image of fabricated high-aspect-ratio nm-AuPNPs is approximately 300 nm in diameter and each contains approximately 120-130 hotspots.

Details of the fabrication process are reported in our previous articles.[44-45] After fabrication, we modified the particle surfaces with HS-PEG-COOH to form a covalent bond between nm-AuPNPs and polyethylene glycol (PEG) (Fig. 2 (b)), for better adhesion onto the cell membrane.[46] We detected two peaks at 516 nm and 945 nm as shown in Fig. 2 (c). The absorption band at peaked around 516 nm arises due to interband electronic transitions.[47-49] The peak at 945 nm corresponds to surface plasmon resonance at the gold surface. The plasmon peak position can be tuned by changing the aspect ratio of the particle through either dry etching or thin-film coating methods,[44-45] or wet–chemistry synthesis.[50] Supplementary Fig. S3 shows the corresponding UV extinction spectra of spherical AuPNPs with peaks centered at 522 nm, 630 nm and 730 nm, which completely differs from the nm-AuPNPs spectra. Fig. 2 (d) shows a scanning electron microscopy (SEM) image of nm-AuPNPs attached to the cell membrane surface. The average number of nm-AuPNPs attachment was approximately 50-60 per cell.

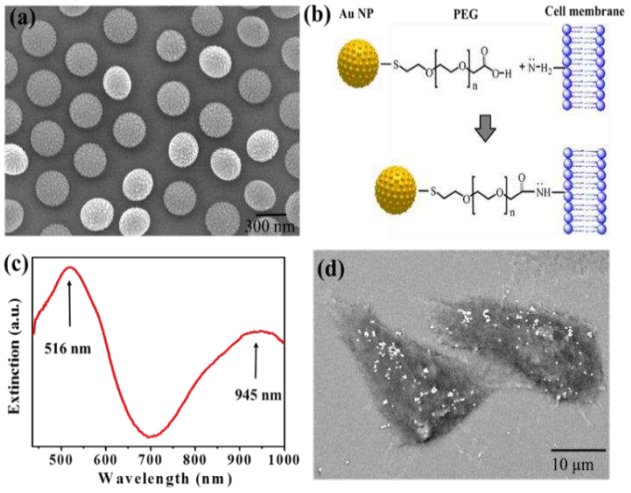

Fig. 2 nm-AuPNPs fabrication and attachment on cell surface (a) SEM image of fabricated nm-AuPNPs (300 nm particle) (b) nm-AuPNPs synthesis and surface modification by using polyethylene glycol (PEG) for strong attachment between nm-AuPNPs and cell membrane (c) the extinction spectra of the

particles have transverse peak (TP) at 516 nm and longitudinal peak (LP) at 945 wavelength (d) SEM image of nm-AuPNPs attachment on lung cancer (CL1-0) cells.

We exposed cells mixed with propidium iodide (PI) dye with spherical AuPNPs (at 522 nm) and asymmetry type nm-AuPNPs (at 516 nm) separately, using the same laser fluence (25 mJ/cm^2) for 30 seconds at 10 Hz pulse frequency. We found that for CL1-0 cells (see supplementary Fig. S5), spherical AuPNPs achieved a maximum of 24% delivery efficiency with 95% cell viability. Also, we examined different cell types by using spherical AuPNPs, as shown in Supplementary Fig. S6, resulting a maximum cellular delivery efficiency of around 17-24% at 522nm. Interestingly, nm-AuPNPs achieved a maximum of 88% delivery efficiency along with 92% cell viability at 516nm (Fig. 4a). This is the direct consequence of higher energy absorption of nm-AuPNPs, which clearly improves delivery efficiency and cell viability compared with spherical AuPNPs.

It is important to note that the best results were found at 945 nm wavelength, which yielded a 94% intracellular PI dye uptake and ~100% cell viability at 35 mJ/cm^2 laser fluence for CL1-0 cells. Following paragraphs will discuss the impact of different experimental parameters only for the excitation wavelength of 945 nm which is the main focus of this study.

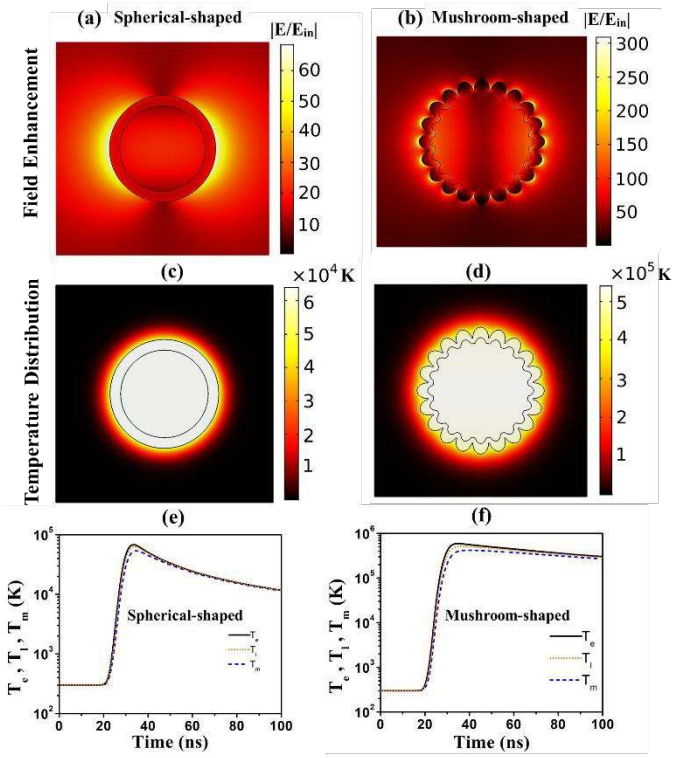

Fig. 3 (a,b)Cross-sectional view of Comsol Multiphysics simulated electric field distribution at 945 nm for spherical (a) and (b) nm-AuPNPs in core –shell configuration with polystyrene as core and Au taken as shell. (c,d) Corresponding temperature distribution when T_l in Au shell reaches the maxima. Temperature outside (inside) the shell corresponds to the distribution of water (polystyrene) temperature T_m (T_c). Excitation pulse energy of ~35 mJ/cm^2 with pulse width of 5 ns was used in this simulation. (e,f) Transient temperature rise at an arbitrary point on gold/water interface for (e) spherical and (f) nm-AuPNPs.

To justify the PNBs as the physical origin of the cell transfection at 945 nm, we have carried out electromagnetic simulations in 3D finite element method by using Comsol Multiphysics software. The model particles are in core-shell configuration where core is the polystyrene and shell is the gold material. The spherical particle has gold coating with thickness of 30 nm on top of spherical polystyrene of size around 280 nm. For mushroom-shaped particle the gold has an average thickness of ~30 nm coated on the corrugated surface of polystyrene. The wavelength dependent complex refractive index ($\mathbf{n} + \mathbf{ik}$) of are taken from Ref. 51 for Au and Ref. 52 for water medium in the simulation. The complex refractive index of polystyrene was kept fix for all wavelengths to $\mathbf{n} + \mathbf{ik} = \mathbf{1.59} + \mathbf{i0.02}$.[53] Fig. 3 shows the cross-sectional view of COMSOL Multiphysics simulated electric field enhancement results of the spherical particle and nm-AuPNPs placed in water for the excitation wavelengths 945 nm. From the simulations, it is clear that plasmonic electromagnetic field enhancement is approximately 4.5 times higher at the edge of the nm-AuPNPs than that of spherical AuPNPs. Usually, a few nm size gold nanoparticle shows plasmonic peak at around 532 nm.[38,39,54] In contrast, the strong field enhancement at 945 nm arises due to the larger size of the particle, which causes electromagnetic retardation and the shifts of the plasmonic peak towards the infrared region.[54,55] The higher enhancement in mushroom-shaped particle occurs because of corrugated surface, which causes nanolocalized plasmonic enhancement in the vicinity of the tips of corrugated surface and the inter-spike nano-space. The field enhanced regions act as plasmonic hot spots and also result in enhancement of Joule heating. As a consequence, the temperature of the gold nanoparticle increases above its initial temperature and diffuses into its surrounding medium. The transient rise of local temperature has been simulated and discussed in the following paragraph.

To obtain temperature rise, we have adapted two temperature model to account the temperature rise of Gold. The pulse laser exposure results in the rise of electron temperature, T_e in gold shell. The increase of T_e leads to the rise of gold lattice temperature T_l as well due to strong electron-phonon coupling. The temperature of the surrounding medium T_m also starts to increase within a few picoseconds due to the transfer of heat from nanoparticle to the adjacent medium. The variation of these temperatures in

View Article Online
DOI: 10.1039/D0NR01702B

time and space are described by the following rate equation model [56]:

$$C_e(T_e)\frac{\partial T_e}{\partial t} = \nabla(k_e \nabla T_e) - g(T_e - T_l) + Q(t) \quad (1)$$

$$C_l\frac{\partial T_l}{\partial t} = \nabla(k_l \nabla T_l) + g(T_e - T_l) - g_l(T_l - T_m) - g_c(T \quad (2)$$

$$\rho_m C_m\frac{\partial T_m}{\partial t} = \nabla(k_m \nabla T_m) + g_l(T_l - T_m) \quad (3)$$

$$\rho_c C_c\frac{\partial T_c}{\partial t} = \nabla(k_c \nabla T_c) + g_c(T_l - T_c) \quad (4)$$

where $C_e(T_e) = \gamma T_e$, with $\gamma = 70\ \mathrm{J m^{-3} K^{-2}}$ is the electron heat capacity for gold [56], $C_l = 3 \times 10^6 \mathrm{J m^{-3} K^{-1}}$ is lattice heat capacity of gold [56], $k_e = 300\ \mathrm{W m^{-1} K^{-1}}$ for the electron thermal conductivity [56]; $k_l \sim 2.7\ \mathrm{W m^{-1} K^{-1}}$ for the lattice thermal conductivity[57]; g = 2.0 × 10^{16} $Wm^{-3}K^{-1}$ for gold electron-phonon coupling coefficient [56]; $C_m = 4182\ \mathrm{J m^{-3} K^{-1}}$ the water heat capacity[56]; $k_m = 0.6\ \mathrm{W m^{-1} K^{-1}}$ for the water thermal conductivity[56]. The terms $g_l(T_l - T_m)$ in Eqs. 1 - 4 represent the boundary interface heat exchange between the gold lattice and the surrounding water, where $g_l = 105 \times 10^6\ Wm^{-2}K^{-1}$ are the corresponding thermal boundary conductance[56]. The terms $g_c(T_l - T_c)$ in Eqs. 1 - 4 represent the boundary interface heat exchange between the gold lattice and the polystyrene core, where $g_c = 508 \times 10^6\ Wm^{-2}K^{-1}$ is interface (gold/polystyrene) thermal conductance calculated following Eq. 5 in Ref. 58,59. In Eq. 1, the source term $Q(t)$ is defined by the transient resistive heating due to a 5 ns Gaussian laser pulse excitation at the fluence of 35 mJ/cm^2. The above equations do not include any phase change phenomena due to the rise of temperature. The spatial distribution of the temperature at peak position (at the point where T_l reaches its maximum value) is shown in Fig. 3c and Fig 3d. The transient dynamics of T_e, T_l, and T_m at an arbitrary interface point (where the field enhancement is maximum) are shown in Fig. 3e for spherical particle and Fig. 3f for mushroom-shaped particle. Again, all the transient simulations were done by using 3D Comsol Multiphysics.

It is worth noting that T_e and T_l increase synchronously for both particles, and T_l reaches the melting temperature (~1337 K) and the boiling temperature (~3129 K) of bulk gold at the early stage of the arrival of the laser pulse.[60,61] Thus, though the simulation results show that T_e and T_l increase far above the melting temperature of gold, in practice, the real values cannot exceed the boiling temperature of bulk gold (~3129K).[62] Therefore, it is very likely to obtain particle deformation, surface melting, and evaporation followed by the size-reduction of the gold nanoparticles for both shapes.[62] Lambard et al. also estimated that cavitation bubbles start to generate when the lattice temperature of gold at gold/water interface rises above a certain critical temperature- named as spinodal temperature, T_{spin} ~550 K.[61] Therefore we expect the generation of plasmonic cavitation bubbles surrounding the nanoparticle/water interface. According to the above simulations, those phenomena are more likely to occur in mushroom-shaped particles compare to spherical shaped particles because the temperature rise is around one order of magnitude higher in the former one (Fig 3(c-f)). The post pulses (2nd, 3rd ...so on) will act on the deformed shaped particles and reduce the probability of temperature rise and bubble generation. However, during these processes, whenever T_l becomes more than 550°C, bubble generation will occur at the gold/water interface.[61] The experimental visualization of bubble formation and its temporal dynamics at each step after pulse excitation is beyond the scope of the present work. All these results reinforce the claim of dynamic plasmonic bubbles to be the origin cell poration at 945 nm.

Parameters to control delivery efficiency and cell viability

Nm-AuPNPs concentration

To determine the highest delivery efficiency and cell viability results for PI dye uptake, we tested different concentrations of nm-AuPNPs. We reported optimum delivery efficiency, and cell viability by using: 1.75×10^{11} particles/mL at 30-35 mJ/cm^2 laser fluence with 10 Hz pulse frequency for 30 seconds laser exposure at 945 nm for CL1-0, AGS, and P-19 stem cells. We found that increasing particle concentrations above 1.75 × 10^{11} particles/mL, reduced delivery efficiency and cell viability (Fig. S7). As shown in Fig. S8, higher concentrations of nm-AuPNPs (3.8×10^{11} particles/mL) produced more debris (bright-field image after laser exposure) and dramatically reduced cell viability (calcein-AM for live cell staining) and delivery efficiency of PI dye (Fig. S8 (c, d)). Moreover, when we introduced pulsed lasers (30 mJ/cm^2 for 30 seconds with 10 Hz pulse frequency) on AGS cells without nm-AuPNPs, we reported no uptake of PI dye into the cells (Fig. S9). Therefore, appropriate particle concentrations play an important role in intracellular delivery.

The control experiment and toxicity test results were provided in Fig. S10 for CL1-0 cells, where pulse laser was exposed on first day with nm-AuPNPs and then cell viability was tested on different days. The results show that, most of the cells are viable after three days.

Exposure time

Supplementary Fig. S11 shows the delivery efficiency and cell viability into CL1-0 cells as a function of laser exposure time, using 35 mJ/cm^2 laser fluence at 945 nm. We reveal that increasing exposure times to 30 seconds, increases the delivery efficiency to a maximum of ~94%, and cell viability to ~100%; above this exposure time, both delivery efficiency and cell viability began to decrease.

Laser fluence and wavelength

View Article Online
DOI: 10.1039/D0NR01792B

Fig. 4 shows the effect of laser fluence on intracellular delivery efficiency and cell viability of CL1-0 cells at 516 nm and 945 nm with 30-second laser exposures (Fig. S12 shows the data for AGS and P-19 stem cells at 945 nm). Upon increasing laser fluence at 516 nm, we achieved the highest delivery efficiency of 88% and 92% cell viability at 25 mJ/cm^2, which then decreased with further laser fluence increases. At 945 nm, the maximum delivery efficiency was 94%, with ~100% cell viability at 35 mJ/cm^2 laser fluence.

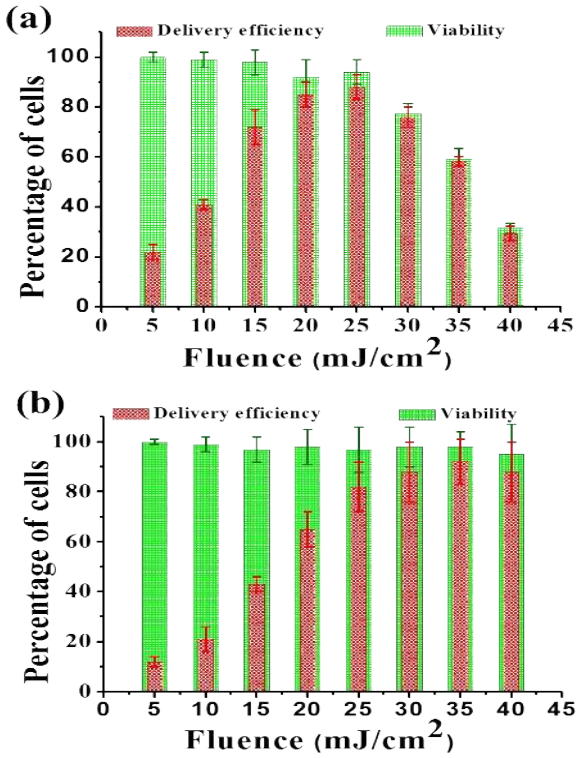

Fig. 4. Effect of nanosecond pulse laser fluence on intracellular delivery efficiency and cell viability of CL1-0 cells at 516 nm and near-infrared at 945 nm wavelength under nm-AuPNPs mediation (a) the delivery efficiency and cell viability at 516 nm with different laser fluence. (b) the delivery efficiency and cell viability at 945 nm laser excitation with different laser fluences. Data show the average ± standard deviation (n = 3 replicate).

Our results demonstrate that delivery efficiency and cell viability at 945 nm is higher than at 516 nm. To confirm these results, we also tested a non-resonant wavelength at 660 nm (Fig. S13), where PI dye delivery was not achieved, indicating no cell poration. However, a very few cells showed red fluorescence imaging (Fig. S13 b, f, j) indicating the nucleus of dead cells.

The maximum power density limit of illumination was 25 mJ/cm^2 for 516 nm. Fig. S14 shows PI dye delivery and viability of CL1-0 cells at 50 mJ/cm^2 laser fluence with a 10 Hz pulse frequency for 30-second laser exposure at 516 nm. The results clearly show that most of the cells are dead at higher laser fluence (bright field Fig. S14a); only about 3.7% of cells were viable.

Here, it is worth noting that a previous study on cell opto poration induced by plasmonic nanobubbles generated through pulsed laser heated Au nanoparticles required much higher fluence (~0.38 J/cm^2 -2.05 J/cm^2) to achieve successful cell poration.[37] This study used 70 nm spherical Au nanoparticles in the experiments. [37] There are several studies showing field enhancement ($|E/E_{in}|$) in the range of 6-8 for similar size (60-80nm) Au nanoparticles,[63,64] which is around 10 times lower than the spherical particle (Fig. 3a) and around 14 times lower than the nm-AuPNPs (Fig 3b) used in our study at 945nm. Therefore absorption efficiency and the heating effect would be much higher in the later particles resulting in lower threshold fluence (E_{PNB}) for the generation of PNBs. In addition, the increase of particle size in core-shell configuration reduces the E_{PNB} as per previous studies by Lukianova-Hleb et al.[65] It showed E_{PNB} is lower in core-shell structure compare to same size all-Au spherical particle. [65] For example, E_{PNB} for 250 nm solid Au sphere was ~100 mJ/cm^2 whereas ~40 mJ/cm^2 for silica@gold shell at 532 nm. [65] It is also important to note that bigger size particle shifts central wavelength for plasmonic resonance towards infrared region. Thus, at resonant excitation E_{PNB} is expected to be more low value compare to nonresonant excitation. All these previous understandings[65] along with our temperature simulation results readily support our observation of lower threshold fluence for the onset of plasmonic nanobubbles compare to the previous study[37].

Intracellular delivery

Molecular dye delivery

We have used PI dye to test the delivery efficiency at the molecular level. PI dye is cell impermeable, but it delivers into a live cell cytosol, visualized by red fluorescence, only after physical rupture of the cell membrane.[5-6] We added PI dye (~45 µl/ml, Fig. S15 showing delivery efficiency and viability as different dye concentrations) to the dish immediately before we activated the nanosecond-pulsed laser. To test cell viability, we added cell-permeable calcein-AM dye after three hours of laser exposure. Fig. 5 shows successful PI dye delivery into CL1-0, AGS and P-19 embryonic stem cells, which remained highly viable, using 35 mJ/cm^2 laser fluence at 945 nm at 10 Hz pulse frequency for 30 seconds. Fig. 5 (a, d, g) show successful PI dye delivery into the CL1-0, AGS and P-19 stem cells, respectively, whereas Fig. 5 (b, f, h) show the corresponding live cells (calcein-AM staining) after PI dye delivery and Fig. 5 (c, f, i) show the merged images of PI dye delivery and live-cell imaging.

View Article Online
DOI: 10.1039/D0NR01792B

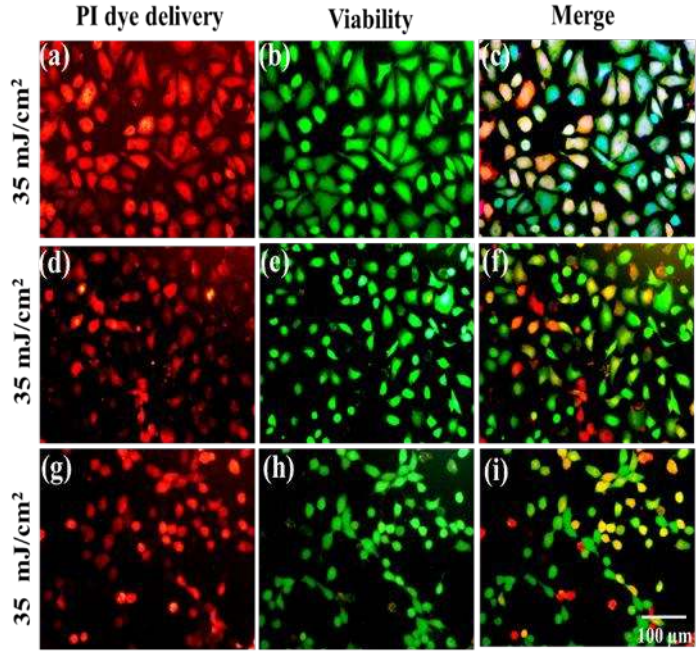

Fig. 5 nm-AuPNPs mediated PI dye delivery into different cell type at 945 nm laser excitation (a) red fluorescence indicating successful PI dye delivery into lung cancer (CL1-0) cells (b) green fluorescence indicating maximum cells are viable by using calcein-AM (c) merged image of PI dye and calcein-AM (d-f) PI dye delivery, cell viability and merge image of gastric cancer (AGS) cells (g-i) PI dye delivery, cell viability and merge image of P-19 embryonic stem cells. Data show the average ± standard deviation (n =3 replicate).

To confirm that nm-AuPNPs effectively delivers PI dye into cells, we conducted area restricted pulse laser exposure on cells with nm-AuPNPs. The results depicted that PI dye is only successfully delivered through the exposed area (Fig. S16 (b)) into CL1-0 cells, and all cells remained viable (calcein-AM staining) after delivery in both exposure and non-exposure areas (Fig. S16 (c)). We observed similar results for AGS and P-19 stem cells, which are shown in Supplementary Fig. S17.

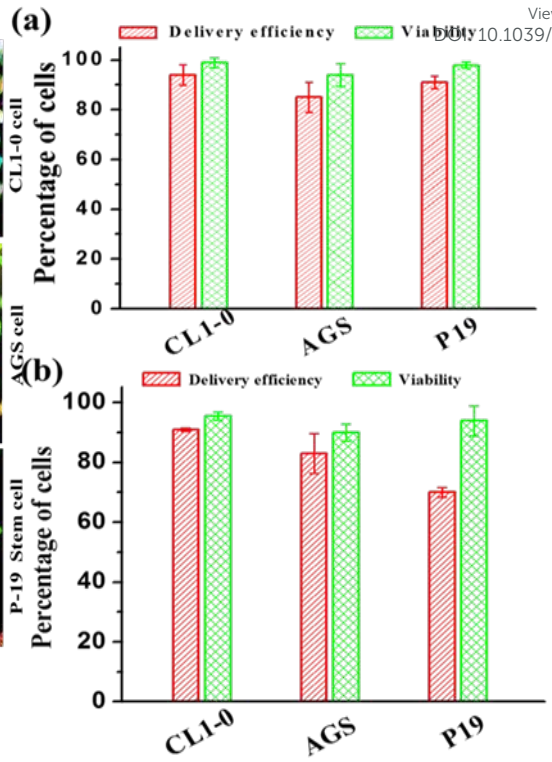

Fig. 6 PI dye and QDs delivery efficiency and cell viability of different cancer cells and one stem cell at 945 nm wavelength (a) The PI dye delivery efficiency (92%) and viability (~ 100%) were higher for CL1-0 cells, whereas the delivery efficiency (86%) and viability (95%) were lower for AGS cells (b) QDs delivery efficiency and viability for deferent cells, where maximum efficiency (89%) and viability (95%) were found for CL1-0 cells and lower delivery efficiency (70%) with higher viability (94%) for P-19 stem cells. For both cases, the laser exposure was 30 seconds at 10 Hz pulsing frequency with 35 mJ/cm^2 laser fluence. Data show the average ± standard deviation (n =3 replicate).

Fig. 6 (a) shows the delivery efficiency and cell viability at 945 nm, where we recorded maximum delivery efficiency of 94% with ~100 % cell viability of CL1-0 cells. For AGS and P-19 cells, the delivery efficiency was 85% and 91%, respectively, while cell viability was 94% and 98%, respectively. In general, we found cell viability was higher at 945 nm, compared with those at 516 nm (see Fig. S18-S19). The best results at 516 nm were achieved with 88% efficiency and 94% viability for CL1-0 cells (Fig. S19). For AGS and P-19 stem cells, 81% and 84% efficiency were achieved with 85% and 88% cell viability, respectively (Fig. S19). On the other hand, we tested spherical AuPNPs which required ~120 mJ/cm^2 laser fluence at 630 nm (Fig. S20) and ~110 mJ/cm^2 laser fluence at 730 nm (Fig. S21) for 30 seconds. From these results, it is clear that the energy requirement is almost 3-4 times higher for spherical AuPNPs compare to nm-AuPNPs.

QDs delivery

To examine the delivery efficiency of nanoparticles such as QDs, using nm-AuPNPs, we initially washed unbound nm-AuPNPs from the cell dish using PBS solution, before introducing $CdSxSe_{1-x}$ / ZnS core nanocrystals coated with COOH functional ligands into the cell dish. After laser exposure, we immediately washed the QDs from the dish and introduced cell culture medium (DMEM for CL1-0 and AGS; MEM for P-19 cells) into the dish for cell imaging. Fig. 6b shows the QDs delivery efficiency and cell viability of different cancer cells and one type of stem cell.

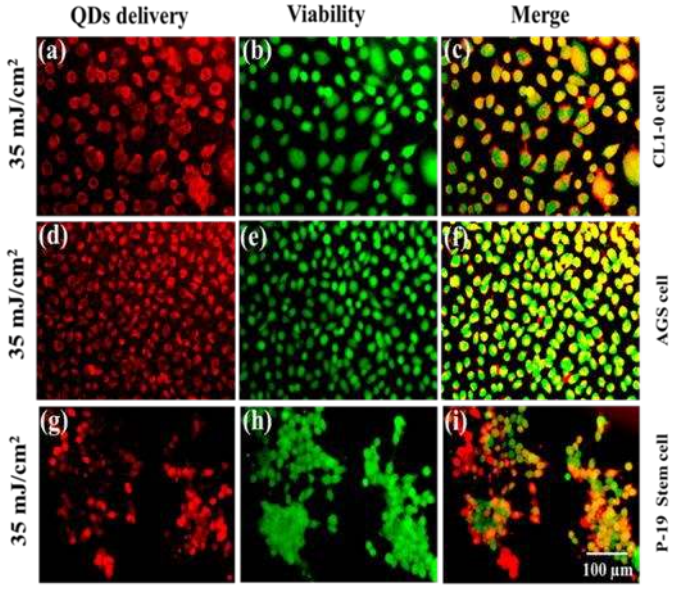

Fig. 7 QDs delivery and cell viability for CL1-0, AGS and P-19 embryonic stem cell at 945 nm wavelength (a) red fluorescence indicating successful QDs delivery into lung cancer (CL1-0) cells (b) green fluorescence indicating all cells viable by using calcein-AM (c) merge image of QDs and calcein-AM (d-f) QDs delivery, cell viability and merge image of gastric cancer (AGS) cells (g-i) QDs delivery, cell viability and merge image of P-19 embryonic stem cells. For each Data show the average ± standard deviation (n = 3 replicate).

Fig. 7 shows fluorescence images of QDs delivery and describes cell viability of CL1-0, AGS, and P-19 embryonic stem cell at 35 mJ/cm² laser fluence with 945 nm laser excitation at 10 Hz pulse frequency for 30 seconds. Fig. 7a shows QDs delivery for CL1-0 cells exhibited 91% delivery efficiency and 95% cell viability (see Fig. 6b). The calcein-AM staining of live cells in Fig. 7b indicates that the majority of the cells remained viable after QDs delivery. The merged image of QDs delivery and live cell staining is shown in Fig. 7c, which indicated that QDs delivered into cells. For AGS cells and P-19 stem cells, the delivery efficiency was 83% and 70%, respectively, and cell viability was 90% and 94%, respectively. The QDs were about 5.5–6.5 nm in size, whereas the PI dye was approximate 0.69 nm in diameter and 1.55 nm in length (cylindrical approximation). Therefore, the lower delivery efficiency of the QDs compared with the PI dye is due to its larger molecular size and weight, resulting in a lower diffusion rate. Fig. S22 shows QDs delivery on the non-exposure area of CL1-0, AGS cells, and P-19 stem cells at 945 nm with 35 mJ/cm² laser fluence for 30 seconds. The results clearly show that in non-exposure areas, QDs were not delivered into different cancer cells and stem cells (Fig. S22 c, g, k), and the cells remained viable (Fig. S22b, d, h, i).

Plasmid delivery with dose control

For efficient plasmid delivery, we used two different plasmids, pMax-E2F1, and pCAG-GFP. For these experiments, after washing unbound nm-AuPNPs from the cell surface, we added different concentrations of the plasmids into the cell culture dish, before exposing laser pulses at 40 mJ/cm² laser fluence with 945 nm at 10 Hz pulse frequency for 30 seconds. We achieved enhanced cell viability at 945 nm, and thus, we performed all plasmid delivery experiments at this wavelength. After laser exposure and before cell incubation, we washed all residual plasmids from the cell culture dish and added the required fresh medium onto the dish. Then approximately 30 h later, we captured the final protein expression image. Fig. 8 (a) shows the dose control transfection efficiency and cell viability for CL1-0, AGS and P-19 stem cells. For pMax-E2F1, at 71.81 ng/µL plasmid concentration, the maximum transfection efficiency occurred using CL1-0 cells, which reached 86% with 96% cell viability. Fig. 8 (b, c) shows confocal scanning images for pMax-E2F1 and pCAG-GFP delivery and GFP expression results using CL1-0 cells, whereas Fig. 8 (d, e, f, g) show GFP expression of AGS and P-19 stem cells. Fig. 8 (h, i) shows the transfection efficiency and cell viability of CL1-0, AGS and P-19 stem cells using pMax-E2F1 and pCAG-GFP at 945 nm pulse laser excitation under nm-AuPNPs mediation. For pMax-E2F1, we achieved 82% and 73% transfection efficiency, and 98% and 96% cell viability, for AGS and P-19 stem cell, respectively. While for pCAG-GFP, we achieved 79%, 81%, and 63% transfection efficiency, and 92%, 96% and 94% cell viability, for CL1-0, AGS and P-19 stem cells, respectively.

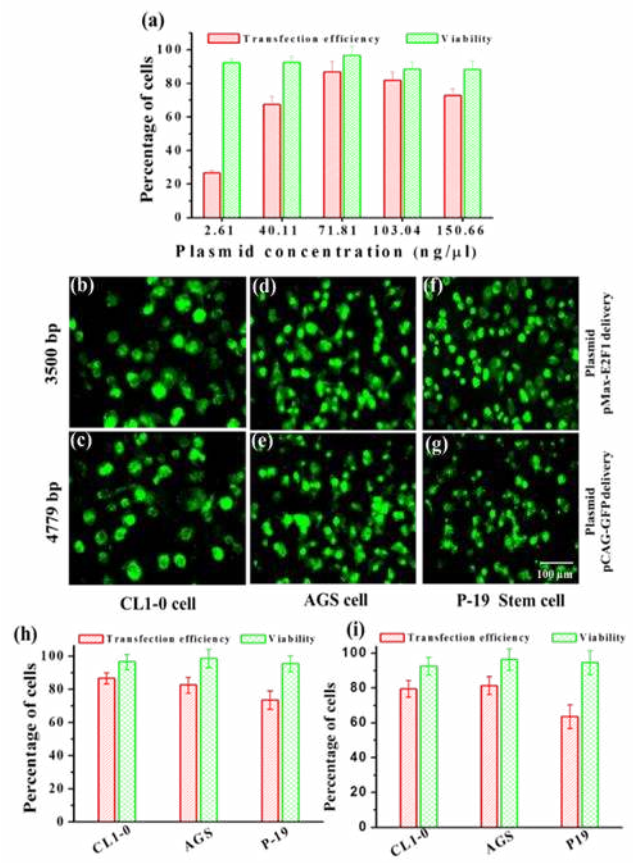

Fig. 8 Doses control, transfection efficiency, cell viability and confocal scanning images of plasmid delivery for GFP expression of CL1-0, AGS and P-19 stem cell at 945 nm wavelength (a) transfection efficiency and viability of CL1-0 cells for pMax-E2F1 delivery with different plasmid concentrations (b & c) confocal scanning images of pMax-E2F1 and pCAG-GFP plasmid delivery and protein expression of CL1-0 cells after 24 hours (d & e) pMax-E2F1 and pCAG-GFP plasmid delivery and protein expression of AGS cells after 24 hours (f & g) pMax-E2F1 and pCAG-GFP plasmid delivery and protein expression of P-19 embryonic stem cells after 24 hours (h) transfection efficiency and cell viability using pMax-E2F1 of CL1-0, AGS and P-19 stem cells (i) transfection efficiency and cell viability using pCAG-GFP of CL1-0, AGS and P-19 stem cells. Data show the average ± standard deviation (n =3 replicate).

We examined both plasmids for delivery in laser exposure and non-exposure areas, as shown in Fig. S23-S24. The results demonstrate successful plasmid delivery occurred only into the exposure areas. Noteworthy, using our nm-AuPNPs mediated photoporation process, traditionally hard to transfect cells, such as stem cells (currently P-19 cells) can be successfully transfected with plasmids at an efficiency of 63% and 73%, for pCAG-GFP and pMax-E2F1, respectively, which has tremendous potential in the delivery of nano-objects into cells.

Cell viability test

The viability of cells was assessed via (MTT), 3-[4,5-dimethylthiozol- 2-yl]-2,5 diphenyl tetrazolium bromide (SRL, Mumbai, India) assay for HCT-8 and HeLa cell lines. Briefly, 5000 cells were seeded in 96 well plates (Tarsons, India) along with 20µl nanoparticles and 180µl of DMEM high glucose medium (Gibco™) in sterile conditions.

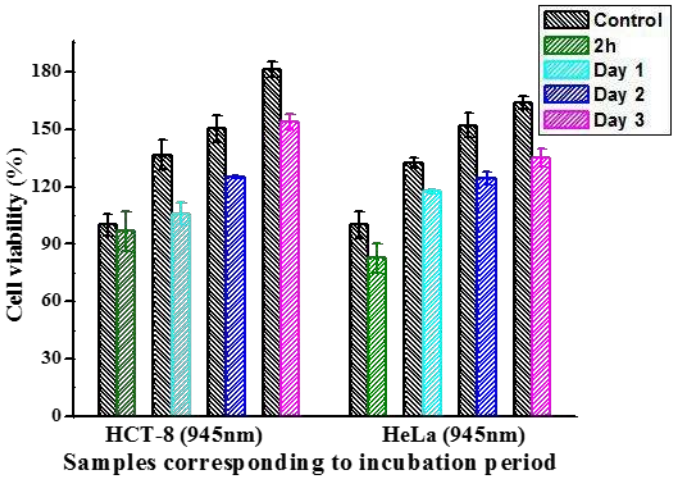

Fig.9 Cell viability of HCT-8 and HeLa cells using MTT assay on different days after laser exposure at 945nm wavelength corresponding to 35 mJ/cm^2 energy for the 30s each.

After overnight incubation at 37 ^{0}C with a 5% CO_2 incubator, the cultured cells were exposed using pulsed laser using 522 nm and 945nm wavelength corresponding to 35 mJ/cm^2 energy for the 30s each (Fig. S25 shows viability results using MTT assay at 516 nm wavelength). Afterward, cells were washed with PBS and then cell culture media was changed at alternate days. The MTT assay was performed after 2 h, 1 day, 2 days and 3 days of laser exposure. For each MTT experiment, 30 µl of 10 mg/ml MTT was added to the individual well followed by 4 h incubation at 37 ^{0}C. After incubation in dark for 4h, the medium containing MTT dye was removed and 100 µl of DMSO (SIGMA, India) was added for dissolving the formazone crystals formed after adding MTT dye. Then the optical density of formazone dissolved DMSO was measured at 570 nm using ELISA plate reader. The measured optical density corresponds to the viability of cells, higher the optical density, greater is the cell viability.

Experimental

nm-AuPNPs fabrication

We considered 510 nm diluted polystyrene (PS) beads as the base templates, which are arranged as dense-packed monolayer hexagonal structure on a substrate for receiving the nanofabrication process only on the top side. Supplementary Fig. S1 shows the process step of nm-AuPNPs

fabrication. Initially, the substrate was cleaned by the piranha solution with a 7:1 ratio of sulfuric acid (H_2SO_4) and hydrogen peroxide (H_2O_2) at 80^0C for 10 minutes. After that, the substrate was treated with oxygen (O_2) plasma under 100W RF power, 75 mTorr pressure and 10 sccm oxygen flow rate to prepare the substrate as hydrophilic in nature. Then the substrate boundary was covered by PDMS films with 250 µm in height to form as a wall. The PDMS layer was made by spin coating with 5 g of uncured PDMS at 1000 rpm for 30 seconds onto a 4-inch glass wafer, pre-coated with a 1% Teflon solution and finally heated with 45^0C overnight to form as 250 µm thickness of the layer. Then 3 µg/ml of the PS beads solution was added into the PDMS mounted well. After water evaporation, the close-packed monolayer PS beds started to form, from the center part to the PDMS wall by the combined effect of capillary force and convective force.[66] After peeling off the PDMS well, the sample was etched by reactive ion etching (RIE) to form as nanocorrugated structure on top of the PS beads (Power = 55W, O_2 flow = 5sccm, Time = 260 s, Pressure = 60 mTorr). Then we deposited Ti/Au (8/30 nm) by electron beam evaporation to form final nm-AuPNPs. A detail fabrication process of nm-AuPNPs is described in our previously published articles.[44-45]

Nanoparticle simulation

We simulate electric field enhancement using electromagnetic waves, frequency domain (Radio Frequency Module) in COMSOL Multiphysics. A Gaussian electromagnetic wave is an incident on a nanoparticle to obtain electric field enhancement by using the finite element method with frequency. A structured nanoparticle is designed using Clewin Layout Editor, which is imported into COMSOL Multiphysics and scaled down to the required size. We simulate it for 516 nm and 945 nm wavelength of incident wave with a spot radius equal to 4mm. The plasma frequency of gold-coated nanoparticles was 1.3×10^{16} and the Drude-Lorentz dispersion model is used for the electric dispersion field model. [67]

Cell culture

For nanosecond pulse laser-induced intracellular delivery, we have used three different types of cells - lung cancer CL1-0, gastric adenocarcinoma cell line AGS and P-19 embryonic stem cells. All of these cell lines were originally from the American Type Culture Collection (ATCC, Manassas, VA, USA). Both CL1-0 and AGS cells were cultured in Dulbecco's Modified Eagles Medium (DMEM) supplemented with 1% sodium pyruvate, 1% non-essential amino acids and 1% penicillin-streptomycin (Gibco, USA). While P-19 embryonal carcinoma cells were maintained and cultured according to the culture method of ATCC CRL-1825 from atcc.org. Cells were cultured with Minimum Essential Medium (MEM) (Invitrogen 61100) and supplemented with 10% Fetal bovine serum (BI 04-001-1A), 100 units/ml penicillin/100 ug/ml streptomycin (Invitrogen 15140), 2 mM L-glutamine (Life Technologies 25030081), and 1 mM sodium pyruvate (Life Technologies 11360070). The exposure circumstances were 5% CO_2 and 37 ^{0}C and a subcultivation ratio was 1:10 every 48 hrs. Before the experiment, cells were dissociated from the dish surface with trypsin (0.05 % trypsin-EDTA, GIBCO), and suspended in the regular culture medium at a density of approximately 3×10^6 cells/ml.

Materials (dyes, QDs and plasmids preparation)

The PI dye (P1304MP, Invitrogen, USA), calcein AM (C3099, Invitrogen, USA), Hoechst 33342 (H3570, Invitrogen, USA) and ethidium homodimer (ETHD-1) (E1169, Invitrogen, USA) were purchased from Life Technologies, USA. The Poly (ethylene glycol) 2-mercaptoethyl ether acetic acid (HSC2H4O $(C_2H_4O)nCH_2CO_2H$) (average Mn 3,500) was purchased from Sigma Aldrich, USA, and $cdSxSe_{1-x}$/Zns core/shell nanocrystals coated with COOH functional ligands (Nanocrystals NC665C, size 5.5 ~ 6.5 nm) was purchased from Crystalplex, Pittsburgh, USA. Both the plasmids were purchased from Addgene (www.addgene.com), where pMax-E2F1 (addgene #16007, Cambridge, MA, USA) is 3500 bp and expresses GFP-E2F1 driven by a pCMV promoter. The pCAG-GFP (addgene #11150, Cambridge, MA, USA) is 4779bp and expresses GFP via chicken beta-actin promoter with CMV enhancer. For both plasmid preparation, DH5α E. coli strain was grown overnight in 100ml LB/Ampicillin or LB/Kanamycin medium. The plasmid purification is guided by QIAGEN® plasmid kit midi (#12145).

Particle synthesis with PEG

The Poly (ethylene glycol) 2-mercaptoethyl ether acetic acid (HSC_2H_4O (C_2H_4O) nCH_2CO_2H) was purchased from Sigma Aldrich. For increasing the colloidal stability of nm-AuPNPs, it was encapsulated with HS-PEG-COOH (Molecular weight 3500 g/mol) to form nm-AuPNPs@PEG. In summary, 1 mL of gold-coated nanoparticle (1.75×10^{11} particles/mL) aqueous suspension was mixed with 1 mg of thiolate PEG. The concentrated solution of NaOH was used to maintain the pH of the solution around 12.0. The reaction mixture was left overnight to undergo a ligand-exchange reaction under mild stirring conditions. Then, the reaction mixture was centrifuged twice for 15 min at 9500 rpm and dispersed in 1 ml Milli-Q water. The high disparity and stability of the gold-coated nanoparticles proves the efficient coating with thiolate PEG.[50]

SEM images of cells with nanoparticles attachment

The PEG mediated nm-AuPNPs were introduced into the cell culture dish and then (after two hours) we washed out unbound nm-AuPNPs from the cell membrane by using phosphate buffer saline (PBS). After that, samples were treated with a different combination of distilled water (DI) and ethanol and then, it was treated again with different ratios of ethanol and hexamethyldisilazane (HMDS). Finally, samples were treated with 100% HMDS and left it for evaporation into the fume hood overnight. After evaporation, we dried the samples at 50^0C for two hours and coated 5nm gold on top of the cells. Finally the SEM (Hitachi TM-1000, version = 03-02, magnification = 3000, working distance = 5880 µm) images were captured.

Conclusions

This study proposes that nm-AuPNP mediated photoporation by employing nanosecond laser pulses enhances intracellular delivery efficiency and cell viability. The asymmetrical nature of nm-AuPNPs raises 120~130 fold higher hotspots compared to spherical AuPNPs, allowing to harvest more laser energy at 516 nm and 945 nm due to plasmon resonance. This leads to the generation of local heat and subsequent formation of PNBs, which induce a strong fluid flow at the nm-AuPNPs-cell membrane interface, creating transient membrane pores that gently deliver exogenous cargos from outside to inside of the cell. We found this method allowed successful delivery of dyes, QDs and plasmids with high delivery efficiency and high cell viability for different cancer cells and stem cells. For PI dye uptake into CL1-0 cells, the lower laser fluence (35 mJ/cm^2) at 945 nm with low nanoparticle concentrations (50-60 nm-AuPNPs/cell) effectively enhanced delivery efficiency up to 94% with ~100% cell viability. For pMAX-E2F1 plasmid delivery, we successfully achieved 86% and 73% delivery efficiency, and 96% and 96% cell viability, for CL1-0 and P-19 stem cells, respectively. Moreover, we obtained around 90-95% cell viability three-day after laser exposure. This technique is potentially beneficial for biological cell research and therapeutic applications.

Conflicts of interest

The authors declare that there are no conflicts of interest.

Acknowledgments

The authors greatly appreciate the financial support from the Wellcome Trust/DBT India Alliance Fellowship under grant number IA/E/16/1/503062, Frontier Research Center on Fundamental and Applied Sciences of Matters, from The Featured Areas Research Center Program within the framework of the Higher Education Sprout Project by the Ministry of Education (MOE 108QR001I5), the Ministry of Science and Technology (MOST) Taiwan ROC through National Nanotechnology and Nanoscience Program under Contract no. 105-2221-E-007-072-MY3, 105-2321-B-007-003, as well as 108-2638-E-007 -001 -MY2 and Excellent University Center for Biomedical Technology, NTHU, 2013-2016. We are also thankful to Dr. Pallavi Gupta and Ms. Kavitha Illath for their experimental help form bio-μ-nano lab at IIT Madras, India

Notes and references

1. D.W.Pack, A.S.Hoffman, S.Pun and P.S.Stayton, Nat. Rev. Drug Discovery, 2005, **4**, 581.
2. D.Luo and M.Saltzman, Nat. Biotechnol. 1999, **18**, 33.
3. L.H.Yin, S.Q.Fu, T.Nanakorn, F.Garcia-Sanchez, I.Chung, R.Cote, G.Pizzorno, E.Hanania, S.Heimfeld and R.Crystal, Stem Cells, 1998, **16**, 247.
4. R.M.Schmid, H.Weidenbach, G.F.Draenert, S.Liptay, H.L¨uhrs and G.Adler, Gut, 1997, **41**, 549.
5. T.S.Santra, P-C.Wang, H-Y.Chang and F-G.Tseng, Appl. Phys. Lett. 2013, **103**, 233701.
6. T.S.Santra and F-G.Tseng, Micromachines. 2013, **4(3)**, 333.
7. K.K.Ewert, A.Ahmad, N.F.Bouxsein, H.M.Evans and C.R.Safinya, Methods Mol. Biol. 2008, **433**, 159.
8. M.R.Capecchi, Cell, 1980, **22**, 479.
9. D.H.Fuller, P.Loudon and C.Schmaljohm, Methods, 2006, **40**, 86.
10. S.Ohta, K.Suzuki, Y.Ogino, S.Miyagawa, A.Murashima, D.Matsumaru and G.Yamada, Dev. Growth Differ. 2008, **50(6)**, 517.
11. M.D.Lavigne and D.C.Gorecki, Expert Opin. Emerg. Drugs. 2006, **11**, 541.
12. P.Chakravarty, W.Qian, M.A.EI-Sayed Mostafa, EI-Sayed and M.R.Prausnitz, Nature Nanotechnology, 2010, **5**, 607.
13. R.G.Crystal, Science, 1995, **270**, 404.
14. Z.C.Hartman, D.M.Appledorn and A.Amalfitano, Virus Res. 2008, 132**(1–2**), 1.
15. D.Luo and W.M.Saltzman, Nat. Biotechnol. 2000, **18 (1),** 33.
16. S.Mehier-Humbert and R.H.Guy, Adv. Drug Deliv. Rev. 2005, **57**, 733.
17. I.Lentacker, I.De Cock, R.Deckers, S.C.De Smedt and C.T.W.Moonen, Adv. Drug Delivery Rev. 2014, **72**, 49.
18. K.Kim, J.A.Kim, S-G.Lee and W.G.Lee, Nanoscale. 2012, **4**, 5051.
19. J.A.Kim, K.Cho, M.S.Shin, W.G.Lee, N.Jung, C.Chung and J.K.Chang, Biosens. Bioelectron. 2008, **23**, 1353.
20. U.K.Tirlapur and K.Konig, Nature. 2002, **418**, 290.
21. J.Baumgart, L.Humbert, E.Boulais, R.Lachaine, J.J.Lebrun and M.Meunier, Biomaterials. 2012, **33**, 2345.
22. A.Uchugonova, K.Konig, R.Bueckle, A.Isemann and G.Tempea, Opt. Express. 2008, **16**, 9357.
23. D.J.Stevenson, F.J.Gunn-Moore, P.Campbell and K.Dholakia, J.R.Soc. Interface, 2010, **7**, 863.
24. A.V.Nikolskaya, V.P.Nikolski and I.R.Efimov, Cell Commun. Adhes. 2006, **13**, 217.
25. H.Schneckenburger, A.Hendinger, R.Sailer, W.S.Strauss and M.J.Schmitt, Biomed. Opt. 2002, **7**, 410.
26. A.Sengupta, S.C.Kelly, N.Dwivedi, N.Thadhani and M.R.Prausnitz, ACS Nano, 2014, **8(3),** 2889.
27. Z.G.Li, A.Q.Liu, E.Klaseboer, J.B.Zhang and C.D.Ohl, Lab Chip, 2013, **13**, 1144.
28. X.Huang, P.K.Jain, I.H.El-Sayed and M.A.El-Sayed, Nanomedicine, 2007, **2(5),** 681.
29. Z.P.Qin and J.C.Bischof, Chem. Soc. Rev. 2012, **41**, 1191.
30. J.Chen, B.Wiley, Z-Y.Li, D.Campbell and F.Saeki, Adv. Mater. 2005, **17**, 2255.
31. T.S.Santra, F-G.Tseng and T.K.Barik, J. Nanophramacetics and Drug Delivery, 2014, **2**, 1.
32. Y.Lu, G.L.Liu, J.Kim, Y.X.Mejia and L.P.Lee, Nano Lett. 2005, **5**, 119.
33. C-H.Chou, C-D.Chen and C.R.C.Wang, J. Phys. Chem. B. 2005, **109**, 11135.
34. E.Y.Lukianova-Hleb, M.B.G.Mutonga and D.O.Lapotko, ACS Nano, 2012, **6**, 10973.
35. E.Y.Lukianova-Hleb, X.Y.Ren, J.A.Zasadzinski, X.W.Wu and D.O.Lapotko, Adv. Mater. 2012, **24**, 3831.
36. E.Y.Lukianova-Hleb, D.S.Wagner, M.K.Brenner and D.O.Lapotko, Biomaterials, 2012, **33**, 5441.
37. R.Xiong, K.Raemdonck, K.Peynshaert, I.Lentacker, I.D.Cock, J. Demeester, S.C.De Smedt, A.G.Skirtach and K.Braeckmans, ACS Nano. 2014, 8 **(6),** 6288.
38. D. Lapotko, E. Lukianova, A. Shnip, G. Zheltov, M.

Potapnev, A. Oraevsky, V.Savitskiy, and O.Klimovich, Proc. SPIE, 2005, **5697**, 82-89.
39. D. Lapotko, E. Lukianova, M. Potapnev, O. Aleinikova, and A. Oraevsky, Proc. SPIE, 2006, **6086**, 135-142.
40. A. M. Smith, M. C. Mancini and S. Nie, Nat. Nanotechnol., 2009, **4**, 710–711.
41. R. Weissleder, Nat. Biotechnol., 2001, **19**, 316–317.
42. C.Ungureanu, R.Kroes, W.Petersen, T.A.M.Groothuis, F.Ungureanu, H.Janssen, F.W.B.van Leeuwen, R.P.H.Kooyman, S.Manohar and T.G.van Leeuwen, Nano Lett. 2011, **11**, 1887.
43. J.Boneberg, J.Koenig-Birk, H-J.Munzer, P.Leiderer, K.L.Shuford, and G.C.Schatz, Appl. Phys. A, 2007, **89**, 299.
44. H-Y.Hsieh, T-W.Huang, J-L.Xiao, C-S.Yang, C-C.Chang, C-C.Chu, L-W.Lo, S-H.Wang, P-C.Wang, C-C.Chieng, C-H.Lee, F-G.Tseng, J. Mater. Chem. 2012, **22**, 20918.
45. H-Y.Hsieh, J-L.Xiao, C-H.Lee, T-W.Huang, C-S.Yang, P-C.Wang and F-G.Tseng, J. Phys. Chem. C, 2011, **115**, 16258.
46. B.Pelaz, V.Grazu, A.Ibarra, C.Magen, P del. Pino and J.M.de la Fuente, Langmuir, 2012, **28**, 8965.
47. Guo-Ying Yao, Qing-Lu Liu and Zong-Yan Zhao, Catalysts, 2018, **8**(6), 236.
48. M. Guerrisi and R. Rosei, Physical Rev. B, 1975, **12**, 557-563.
49. Lequan Liu, Peng Li, Boonchun Adisak, Shuxin Ouyang, Naoto Umezawa, Jinhua Ye, Rajesh Kodiyath, Toyokazu Tanabe, Gubbala V. Ramesh, Shigenori Ueda, Hideki Abe, J. Mater. Chem. A, 2014, 2, 9875-9882.
50. B.Nikoobakht and M.A.El-Sayed, Chem. Mater. 2003, 15 (10), 1957.
51. P. B. Johnson and R. W. Christy, Phys. Rev. B, 1972, **6**, 4370.
52. G. M. Hale and M. R. Querry, Appl. Opt., 1973, **12**, 555.
53. R. H. French, K. I. Winey, M. K. Yang and W. Qiu, Aust. J. Chem., 2007, **60**, 251–263.
54. P. K. Jain, K. S. Lee, I. H. El-Sayed and M. A. El-Sayed, J. Phys. Chem. B, 2006, **110**, 7238–7248.
55. D. Werner and S. Hashimoto, J. Phys. Chem. C, 2011, **115**, 5063–5072.
56. A. Hatef, S. Fortin-Deschênes, E. Boulais, F. Lesage and M. Meunier, *Int. J. Heat Mass Transf.*, 2015, **89**, 866–871.
57. Y. Wang, Z. Lu, and X. Ruana, Journal of Applied Physics, 2016, **119**, 225109.
58. G. Chang, F. Sun, J. Duan, Z. Che, X. Wang, J. Wang, M. J. Kim and H. Zhang, Acta Mater., 2018, **160**, 235–246.
59. Y. Zhang, H. L. Zhang, J. H. Wu and X. T. Wang, Scr. Mater., 2011, **65**, 1097–1100.
60. D. Werner, A. Furube, T. Okamoto and S. Hashimoto, J. Phys. Chem. C, 2011, **115**, 8503–8512.
61. J. Lombard, T. Biben and S. Merabia, J. Phys. Chem. C, 2017, **121**, 15402–15415.
62. D. Werner and S. Hashimoto, *J. Phys. Chem. C*, 2011, **115**, 5063–5072.
63. J. Shin, M. Song, H. Hafeez, P. J. Jeusraj, D. H. Kim, J. C. Lee et al., Organic Electronics, 2019, 66, 94–101.
64. Z. Starowicz, R. Wojnarowska-Nowak, P. Ozga and E. M. Sheregii, Colloid and Polymer Science, 2018, 296, 1029–1037.
65. E. Lukianova-Hleb, Y. Hu, L. Latterini, L. Tarpani, S. Lee, R. A. Drezek, J. H. Hafner, and Dmitri O. Lapotko, ACS Nano, 2010, 4 (4), 2109–2123.
66. T.Sakai, Y.Takeoka, T.Seki and R.Yoshida, Langmuir, 2007, 23, 8651.
67. C.G.Granqvist and O.Hunderi, Phys. Rev. B, 1977, 16, 3513.

View Article Online
DOI: 10.1039/D0NR01792B